

MIT Open Access Articles

*Antifouling Surface Coatings from Self-Assembled
Zwitterionic Aramid Amphiphile Nanoribbons*

The MIT Faculty has made this article openly available. **Please share**
how this access benefits you. Your story matters.

Citation: Christoff-Tempesta, Ty, Deiss-Yehiely, Elad, Dromel, Pierre C, Uliassi, Linnaea D, Chazot, Cécile AC et al. 2022. "Antifouling Surface Coatings from Self-Assembled Zwitterionic Aramid Amphiphile Nanoribbons." *Advanced Materials Interfaces*, 9 (22).

As Published: 10.1002/admi.202200311

Publisher: Wiley

Persistent URL: <https://hdl.handle.net/1721.1/145734>

Version: Final published version: final published article, as it appeared in a journal, conference proceedings, or other formally published context

Terms of use: Creative Commons Attribution-NonCommercial-NoDerivs License



Antifouling Surface Coatings from Self-Assembled Zwitterionic Aramid Amphiphile Nanoribbons

Ty Christoff-Tempesta, Elad Deiss-Yehiely, Pierre C. Dromel, Linnaea D. Uliassi, Cécile A. C. Chazot, Eveline Postelnicu, A. John Hart, Myron Spector, Paula T. Hammond, and Julia H. Ortony*

Zwitterionic surfaces are increasingly explored as antifouling coatings due to their propensity to resist protein, bacterial, and cell adhesion and are typically applied as polymeric systems. Here, the self-assembly of strongly interacting small molecule amphiphiles is reported to produce nanoribbons for antifouling applications. Synthesized amphiphiles spontaneously form micrometers-long nanoribbons with nanometer-scale cross-sections and intrinsically display a dense coating of zwitterionic moieties on their surfaces. Substrates coated with nanoribbons demonstrate concentration-dependent thicknesses and near superhydrophilicity. These surface coatings are then probed for antifouling properties and substantial reductions are demonstrated in protein adsorption, bacterial biofilm formation, and cell adhesion relative to uncoated controls. Harnessing cohesive small molecule self-assembling nanomaterials for surface coatings offers a facile route to effective antifouling surfaces.

infrastructure,^[8,9] and sustaining materials in marine environments.^[10,11] Currently, harmful biocidal chemicals are used in industrial settings, risking public health and environmental contamination, spurring interest in alternative strategies.^[12–14] Furthermore, the U.S. Centers for Disease Control and Prevention estimates that 1 in 31 U.S. patients has at least one infection during their hospital care via exposure to foreign microbes. These healthcare-associated infections result in close to 100 000 deaths annually.^[6,11,15,16]

Historically, antifouling material design has used hydrophilic surface chemistries to control interactions at the interface between the material and its microenvironment. Rapid adsorption of proteins


(i.e., biofouling) onto a material surface occurs immediately upon exposure to a nonsterile environment, facilitating the attraction of other biological components and determining the material's biological fate and function.^[17,18] Hydrophilic surfaces form a strong hydration layer that inhibits protein adhesion by creating significant energetic penalties to disrupt tightly coordinated solvent interactions, which may be further aided by steric effects.^[19–21] The hallmark example of this application

1. Introduction

The adsorption of biomolecules, microorganisms, and cells to material surfaces is a long-standing challenge for a wide range of biomedical and industrial applications, including preserving safe hospital environments,^[1,2] maintaining sterile medical devices and minimizing degradation-inducing immune responses to implants,^[3–7] reducing impacts to energy

T. Christoff-Tempesta, E. Deiss-Yehiely, P. C. Dromel, L. D. Uliassi, C. A. C. Chazot, E. Postelnicu, J. H. Ortony
Department of Materials Science and Engineering
Massachusetts Institute of Technology
Cambridge, MA 02139, USA
E-mail: ortony@mit.edu
E. Deiss-Yehiely, P. T. Hammond
Koch Institute for Integrative Cancer Research
Massachusetts Institute of Technology
Cambridge, MA 02139, USA

P. C. Dromel
Schepens Eye Research Institute
Mass Eye and Ear
Harvard Medical School
Boston, MA 02114, USA
C. A. C. Chazot, A. J. Hart
Department of Mechanical Engineering
Massachusetts Institute of Technology
Cambridge, MA 02139, USA
M. Spector
VA Boston Healthcare System
Brigham and Women's Hospital
Harvard Medical School
Boston, MA 02130, USA
P. T. Hammond
Department of Chemical Engineering
Massachusetts Institute of Technology
Cambridge, MA 02139, USA
P. T. Hammond
Institute for Soldier Nanotechnologies
Massachusetts Institute of Technology
Cambridge, MA 02139, USA

 The ORCID identification number(s) for the author(s) of this article can be found under <https://doi.org/10.1002/admi.202200311>.

© 2022 The Authors. Advanced Materials Interfaces published by Wiley-VCH GmbH. This is an open access article under the terms of the Creative Commons Attribution-NonCommercial-NoDerivs License, which permits use and distribution in any medium, provided the original work is properly cited, the use is non-commercial and no modifications or adaptations are made.

DOI: 10.1002/admi.202200311

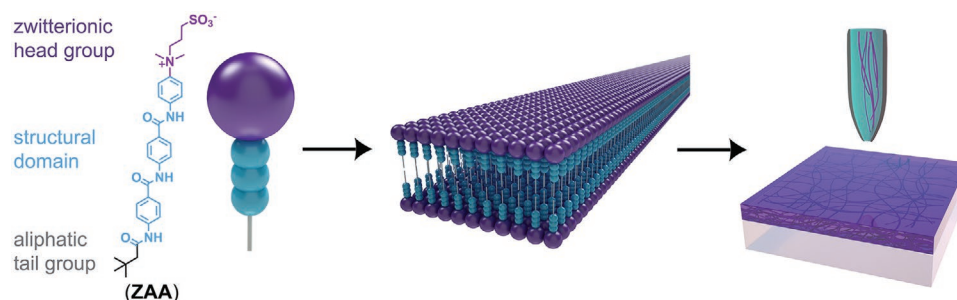


Figure 1. Surfaces coated with zwitterionic aramid amphiphile (ZAA) nanoribbons are resistant to biofouling. Aramid amphiphiles composed of a zwitterionic head group, triaramid structural domain, and hydrophobic tail spontaneously self-assemble in water to form micrometers-long nanoribbons. Suspensions of these stable nanoribbons can be deposited and dried onto surfaces to form a dense nanoribbon mesh that is resistant to biofouling. Molecule and nanoribbon schematic reproduced with permission.^[41] Copyright 2021, Springer Nature.

is the coating of surfaces with poly(ethylene glycol) (PEG) to imbue antifouling properties. These “PEGylated” materials are widely accepted to resist nonspecific protein adsorption, but PEG is susceptible to loss of function in biological milieu from long-term oxidation and requires optimization for grafting to many substrates.^[22–25] An increasing body of evidence also indicates that the nonspecific adsorption of immunogenic proteins on PEG-coated surfaces implanted in vivo can induce the production of PEG-specific antibodies, in turn eliciting rejection of implanted devices.^[26,27]

Zwitterionic chemistries have been increasingly explored as an alternative to PEG-modified surfaces because of their intrinsic capacity to resist biofouling. Zwitterionic materials, composed of molecules with both positive and negative charges, provide a physical and electrostatic barrier to adsorption through robust surface hydration.^[28–31] Polymers containing phosphorylcholine, sulfobetaine, and carboxybetaine zwitterionic moieties have been demonstrated to significantly reduce nonspecific protein adsorption^[22,28,32] and paved the way for research into a growing number of polymeric zwitterionic systems.^[33–35]

Obtaining nanomaterials through small molecule self-assembly offers an alternative approach to polymeric systems for producing zwitterionic-coated surfaces. Amphiphilic self-assembly produces internally organized nanostructures with surface presentations, chemistries, and dynamics that are tunable through molecular design.^[36–40] Importantly, nanomaterials constructed through the self-assembly of zwitterionic small molecule amphiphiles offer extremely high surface densities of zwitterionic moieties that are resistant to biofouling. To this end, we propose that several criteria should be met to form effective antifouling surface coatings from small molecule supramolecular assemblies: 1) the molecular assemblies should be sufficiently stable to maintain their structure upon drying for application; 2) the nanostructures should take on an appropriate geometry for substrate coating and aspect-ratio to provide dense surface coverage; and 3) the surface should produce a substantial hydration layer that is protective against biofouling.

Here, we report the application of supramolecular nanoribbons from zwitterionic aramid amphiphiles (ZAAs) to antifouling surface coatings (**Figure 1**). ZAAs have previously been shown to undergo spontaneous self-assembly in water to form micrometers-long nanoribbons with robust mechanical properties.^[41] To meet the above criteria, we 1) synthesize amphiphiles with a triaramid structural domain—the aramid

amphiphile motif—into the molecular design to tightly coordinate adjacent amphiphiles; 2) select an unobtrusive branched aliphatic tail group to promote assembly into high-aspect-ratio nanoribbons; and 3) incorporate a sulfobetaine head group to form nanostructures with zwitterionic surfaces. This molecular design imparts stability on the resulting self-assembled nanostructures by incorporating a dense network of hydrogen bonds and π -stacking interactions between neighboring molecules. As a consequence, aramid amphiphile-based nanomaterials exhibit suppressed dynamic instabilities relative to conventional small molecule assemblies and realize mechanical properties rivaling silk.^[41] To produce antifouling surface coatings, we self-assemble the ZAAs in water, drop-cast the resulting nanoribbon suspension onto substrates and form thin film coatings via air drying, which we subsequently test for resistance to fouling by proteins, bacteria, and cells.

2. Results and Discussion

2.1. Preparation of Nanoribbon-Coated Surfaces

We prepared ZAAs by first synthesizing the hydrophobic portion of the molecule (aliphatic tail and aramid repeat units) via alternating carbodiimide-mediated coupling reactions and conventional deprotection reactions. We subsequently added the zwitterionic head group through quaternization of a pendant tertiary amine with propanesultone (molecule in **Figure 1**). The protocol to obtain this compound is described in ref. ^[41]. A combination of proton (¹H) nuclear magnetic resonance (NMR) and mass spectrometry were used to characterize the product (see the Experimental Section).

ZAAs spontaneously self-assemble to form micrometers-long nanoribbons in water after 1 h of sonication at room temperature (1 mg mL⁻¹, deionized water), as observed with transmission electron microscopy (TEM, **Figure 2a**). We combine cryogenic transmission electron microscopy (cryo-TEM, **Figure 2b**), atomic force microscopy (AFM, **Figure 2c**), and small angle X-ray scattering (SAXS, **Figure 2d**) to determine the dimensions of the nanoribbon cross-sections. The SAXS profile is best fit to a lamellar model, which defines a nanoribbon thickness of 3.9 nm, and AFM identifies a nanoribbon width of 5.1 nm. These cross-sectional dimensions are corroborated by cryo-TEM and match previously reported dimensions.^[41]

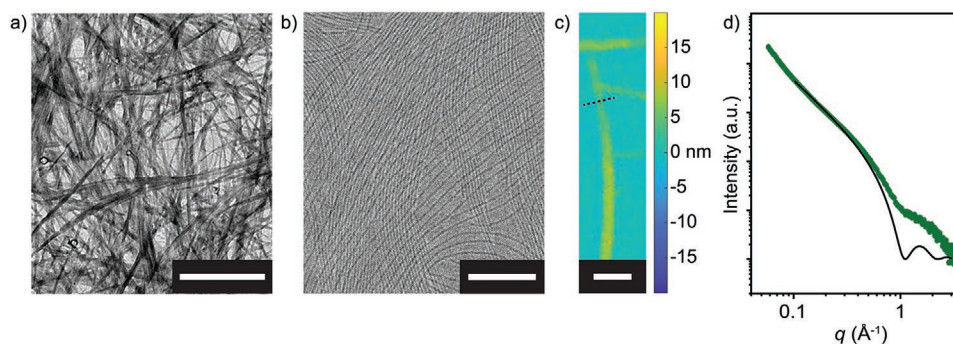


Figure 2. ZAAs form nanoribbons upon self-assembly in water. a) The self-assembly of ZAAs into micrometers-long nanoribbons is observed in transmission electron microscopy. Scale bar: 1 μm . b) Analysis of cryogenic transmission electron microscopy images of the nanoribbons is used to extract $3.9 \times 5.1 \text{ nm}^2$ nanoribbon dimensions. Scale bar: 100 nm. c) Atomic force microscopy corroborates a 5.1 nm nanoribbon width (dotted line). Scale bar: 200 nm. d) Fitting the small angle X-ray scattering profile (green circles) of a ZAA nanoribbon suspension in water to a lamellar model (black line) corroborates a nanoribbon thickness of 3.9 nm.

Aqueous nanoribbon suspensions were deposited and air-dried onto substrates as a simple route to producing antifouling surface coatings. These coatings harness the thermal stability of ZAA nanoribbons, which has been previously demonstrated up to 250 $^{\circ}\text{C}$.^[42] We find with scanning electron microscopy (SEM) that the nanoribbons maintain their 3D architecture, aggregate into bundles, and form a dense mesh (Figure 3a). 250 μL of a 1 mg mL^{-1} nanoribbon solution is observed as the minimum volume needed to fully disperse across 15 mm diameter circular glass discs, which fit the bottom of a 24-well plate. Therefore, we select 250, 300, 500, and 700 μL depositions onto the discs for further analysis, which equates to 1.4, 1.7, 2.8, and 4.0 $\mu\text{g mm}^{-2}$ coatings, respectively. Through surface profilometry, we find that coating thickness linearly increases with coating density ($R^2 > 0.99$), with 1.4, 1.7, 2.8, and 4.0 $\mu\text{g mm}^{-2}$ coatings having average thicknesses of 1.08, 1.24, 1.79, and 2.48 μm , respectively (Figure 3b).

Finally, we employ contact angle goniometry to probe the wetting properties of nanoribbon-coated surfaces (Figure 3c). We hypothesize that the surfaces should be highly wetting due

to the propensity of the zwitterionic moieties to form a hydration layer. The uncoated glass disc control exhibits a water contact angle of $\approx 54^{\circ}$. In contrast, surfaces with ZAA nanoribbon coatings have water contact angles ranging $\approx 13^{\circ}$ – 16° , nearing superhydrophilicity.^[43] The high wettability of the nanoribbon coated surfaces confirm favorable water-nanoribbon interaction.

2.2. Inhibiting Protein Fouling

The instantaneous adsorption of proteins onto the surface of any biomaterial has drastic effects on its downstream performance. Therefore, albumin and lysozyme were initially chosen as model proteins to quantify antifouling. Anionic albumin proteins, measuring $\approx 40 \text{ mg mL}^{-1}$ in blood, are the most prevalent proteins within human serum.^[44] Lysozyme, an innate immune response enzyme, is positively charged at physiologic pH and is commonly used as a representative cationic macromolecule.^[45] Studying antifouling of these two model proteins offers insight

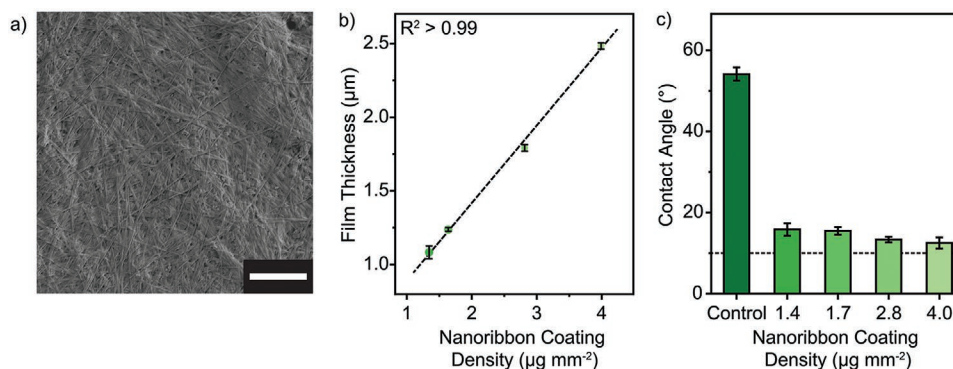


Figure 3. Nanoribbon-coated surfaces show a linear thickness dependence with coating density and are highly wetting. a) A representative scanning electron image of nanoribbon coated surfaces shows maintenance of the 3D structure of the nanoribbons upon drying to form a dense mesh of nanoribbon bundles. Scale bar: 2 μm . b) Profilometry measurements of zwitterionic nanoribbon coatings indicate a linear relationship (dotted line) between coating density and film thickness. Measurements are shown as mean \pm standard deviation ($n = 5$). c) Contact angle measurements as a function of nanoribbon coating density show coated surfaces are highly hydrophilic and offer a significantly lower contact angle than an uncoated glass control. The horizontal dashed line at a 10° contact angle indicates the threshold for superhydrophilicity. Measurements are shown as mean \pm standard deviation ($n = 5$).

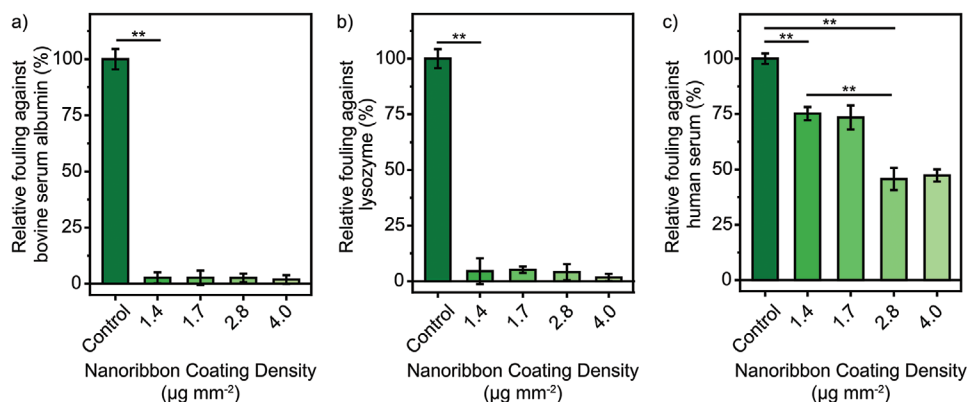


Figure 4. ZAA nanoribbon coatings resist nonspecific protein adsorption. a) The nanoribbon coating reduces bovine serum albumin adsorption 98% relative to an uncoated control, statistically independent of coating density. b) The nanoribbon coating reduces lysozyme adsorption 95–98% relative to an uncoated control, nearly independently of coating density. c) The nanoribbon coating reduces nonspecific protein adsorption from human serum $\approx 25\%$ for 1.4 and 1.7 $\mu\text{g mm}^{-2}$ nanoribbon coatings and $\approx 50\%$ for 2.8 and 4.0 $\mu\text{g mm}^{-2}$ nanoribbon coatings relative to an uncoated control. Data shown as mean \pm standard deviation of $n = 3$ samples for each coating density. Statistical significance determined by a two-tailed Welch's t -test followed by a Bonferroni correction (**, $p < 0.05$ after Bonferroni correction).

into the broad-ranging capabilities of the nanoribbon coatings to prevent fouling from different charges and classes of proteins.

We observe that the nanoribbon surface coating greatly decreases albumin and lysozyme fouling, in line with similar contact angles across thicknesses. Average adsorption values of bovine serum albumin (BSA) on coated substrates range from $\approx 2\%$ to 3% relative to uncoated glass controls (Figure 4a). Similarly, average lysozyme adsorption values range from $\approx 2\%$ to 5% relative to uncoated glass controls (Figure 4b). The nanoribbon coatings also prevent the adsorption of proteins within human serum, a complex system representative of biological environments. Average protein adsorption decreases to between $\approx 47\%$ and 75% fouling relative to uncoated glass controls for human serum incubated on nanoribbon coated surfaces (Figure 4c). The lower effectiveness of the nanoribbon coatings against human serum and its sensitivity to coating thickness is likely influenced by its higher total concentration of proteins ($\approx 60\text{--}80 \text{ mg mL}^{-1}$ in blood,^[46] diluted here 1:10) than in the individual BSA and lysozyme experiments (performed at 1 mg mL^{-1}). Furthermore, smaller proteins and peptides present in human serum may diffuse more easily through the nanoribbon mesh to the glass substrate.^[46]

2.3. Prevention of Bacterial Adhesion and Biofilm Formation

Next, we investigated the adsorption of microbes onto surfaces coated with ZAAs. Bacteria readily colonize abiotic surfaces^[47,48] and adhesion on biomaterials can enable the production of biofilms^[49] that are known to require 100- to 1000-fold increases in antibiotics to eradicate relative to their planktonic, free-swimming counterparts. *Pseudomonas aeruginosa*, a model Gram-negative opportunistic bacterium, is an infamous “ESKAPE” pathogen that poses a dire public health threat.^[50] Notably, its biofilm formation is in part responsible for its antibiotic tolerance, rendering most current therapies ineffective.^[50,51] Reducing surface attachment of microbes, such as *P. aeruginosa*, onto substrates represents a promising solution to inhibit

biofilm production without the use of biocides, negating the most important factor leading toward antibiotic resistance.^[52]

We cultured *P. aeruginosa*, stained in green, for 48 h on an uncoated glass surface and observe a dense attachment of microbes and production of a biofilm matrix (Figure 5a). When we cultured the same bacterium on nanoribbon-coated surfaces, we identify a sensitivity to increasing nanoribbon coating concentrations, whereby fewer and fewer bacteria attach onto the surface (Figure 5b–e). We observe no difference in surface roughness, porosity, morphology, or coverage through profilometry and SEM between substrates with different surface coating densities. Therefore, we attribute this dependence to increasing tortuosity to reach the glass substrate and decreasing adhesion sites for bacterial attachment. By quantifying the biofilm biomass using COMSTAT2,^[53,54] a statistically significant reduction can be observed even with the lowest coating thickness used (Figure 5f). At and above a 2.8 $\mu\text{g mm}^{-2}$ coating, virtually no biofilm biomass is detected, indicating complete surface antifouling.

2.4. Suppression of Cell-Mediated Attachment

Finally, we investigated the prevention of cell attachment to ZAA nanoribbon-coated substrates. We selected the hASC-SVG-p12 cell line, a type of human adipose stem cell (hASC), for this study. hASC-SVG-p12 is a cell line used in a broad range of research, including studies of human immunodeficiency virus and Alzheimer's disease.^[55,56] Notably, this cell line is capable of being cultured directly on uncoated glass substrates with high attachment, viability, and proliferation.

To test for inhibition of cell attachment to nanoribbon-coated surfaces, we cultured hASC on uncoated and nanoribbon-coated discs for three days and analyzed the surface-bound cell number and density using a live-dead assay. The cell density was calculated for live and dead cells, stained in green and red, respectively, with 15 randomly chosen fields in each group. Cells cultured on the uncoated substrate show the highest density as expected (Figure 6a). In contrast, cells cultured on

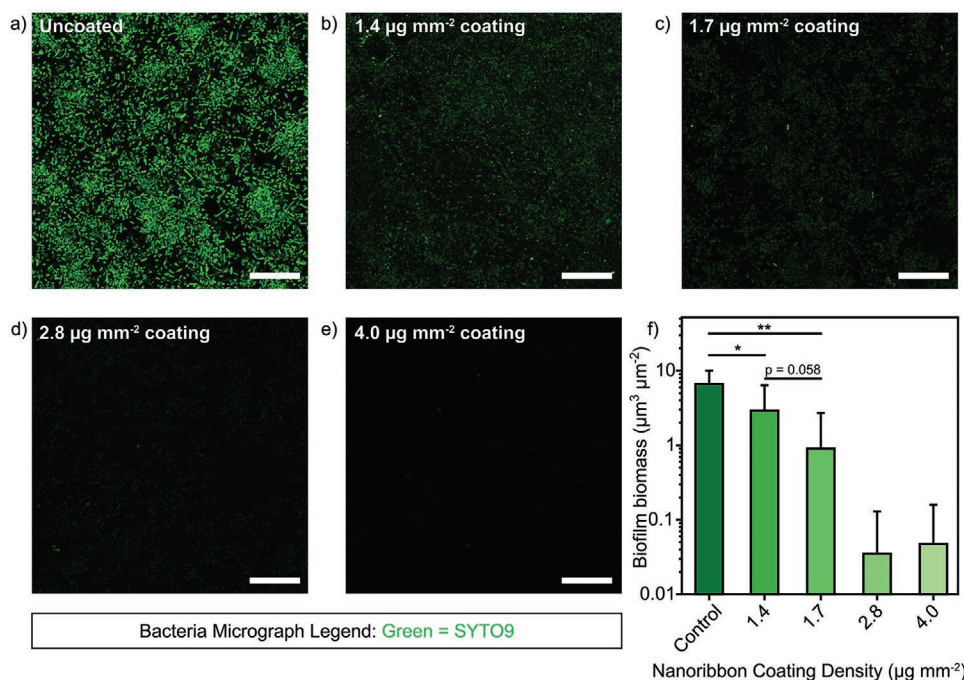


Figure 5. Increasing densities of surface-bound ZAA nanoribbons results in significant reduction of biofilm biomass over 48 h of culturing. a) A representative max intensity z-stack confocal microscope image illustrates microbial (green) adhesion on glass surfaces with no surface treatment. Scale bar: 25 μm . b–e) Representative microscope images demonstrate reductions in biomass with increased concentrations of nanoribbon deposition onto the surface. Scale bar: 25 μm . f) Statistically significant reductions in biofilm biomass are seen at all coating densities tested, as calculated by COMSTAT2.^[53,54] Data shown as mean \pm standard deviation of triplicate wells with five different fields for each well. Statistical significance determined by a two-tailed Welch's *t*-test followed by a Bonferroni correction (*, $p < 0.05$ before Bonferroni correction; **, $p < 0.05$ after Bonferroni correction).

nanoribbon coated-discs demonstrate a significantly lower density (Figure 6b–f). We observe fewer viable cell clusters and dead cells on the nanoribbon-coated surfaces. Of note, we observe a steep decrease in the total cell density from the control group to the less dense nanofiber coating and a coating thickness-dependence to cell density, likely resulting from inhibited diffusion to the glass substrate and lower adhesion sites with increasing coating thicknesses. We also observe that while the total density of dead cells decreases with the addition of a nanoribbon coating, the ratio of dead-to-live cells increases with higher surface coating densities. This indicates some evidence of cytotoxicity which is likely attributed to lowered cell adhesion caused by the coating^[57] and may partially also be attributed to the stiffness of the nanoribbons comprising the coating.^[41]

3. Conclusions

Readily applied coatings which offer protection against the adhesion of biological components are critical to the function of materials in a broad range of application spaces.^[1–16] Harnessing control over the surface chemistry, internal stability, and geometry of supramolecular nanostructures offers a route to produce thin films which minimize nonspecific interactions with biomolecules. In this work, we investigated ZAA nanoribbons which incorporate: a zwitterionic head group to produce a highly hydrated surface; a structural domain to provide internal cohesion; and an optimized geometry to yield high-aspect-ratio nanostructures to significantly reduce biofouling. Upon

addition of water, ZAAs spontaneously formed micrometers-long nanoribbons that maintain structure when dried to readily produce dense nanoribbon mesh coatings. These coatings offered concentration-dependent thicknesses and contact angles approaching superhydrophilicity, indicative of strong nanoribbon-water interactions at the exposed coating surface. These surfaces showed resistance to protein fouling, a two orders of magnitude reduction in bacterial adhesion, and suppressed cell-mediated attachment. The simple strategy to producing water-coordinating surfaces reported here offers insight into extending small molecule self-assembled materials toward effective antifouling coatings.

4. Experimental Section

All materials are from Sigma-Aldrich unless specified otherwise.

Chemical Characterization: Proton (^1H) NMR spectroscopy to analyze the chemical structure of the synthesized amphiphile and intermediates was performed on a Bruker Avance III DPX 400. NMR solutions were prepared by mixing 20 mg of dried sample powder with 500 μL deuterated dimethylsulfoxide ($\text{DMSO-}d_6$). (400 MHz, $\text{DMSO-}d_6$, δ): 10.56 (s, 1H, NH), 10.37 (s, 1H, NH), 10.11 (s, 1H, NH), 8.01 (m, 8H, Ar), 7.88 (d, 2H, Ar), 7.78 (d, 2H, Ar), 3.99 (m, 2H, CH_2), 3.57 (s, 6H, CH_3), 2.42 (t, 2H, CH_2), 1.67 (m, 2H, CH_2), 1.06 (s, 9H, CH_3) ppm.

Mass spectrometry (MS) to confirm the molecular weight of the synthesized zwitterionic aramid amphiphile was carried out on a Bruker Autoflex LRF Speed matrix assisted laser desorption/ionization-time-of-flight (MALDI-ToF) spectrometer. A matrix solution for analysis was prepared by mixing excess ($>10 \text{ mg mL}^{-1}$) α -cyano-4-hydroxycinnamic acid with 500:500:1 solution (by vol.) of deionized water:acetonitrile:trifluoroacetic acid, vortexing for 30 s, centrifuging for 1 min, and retaining

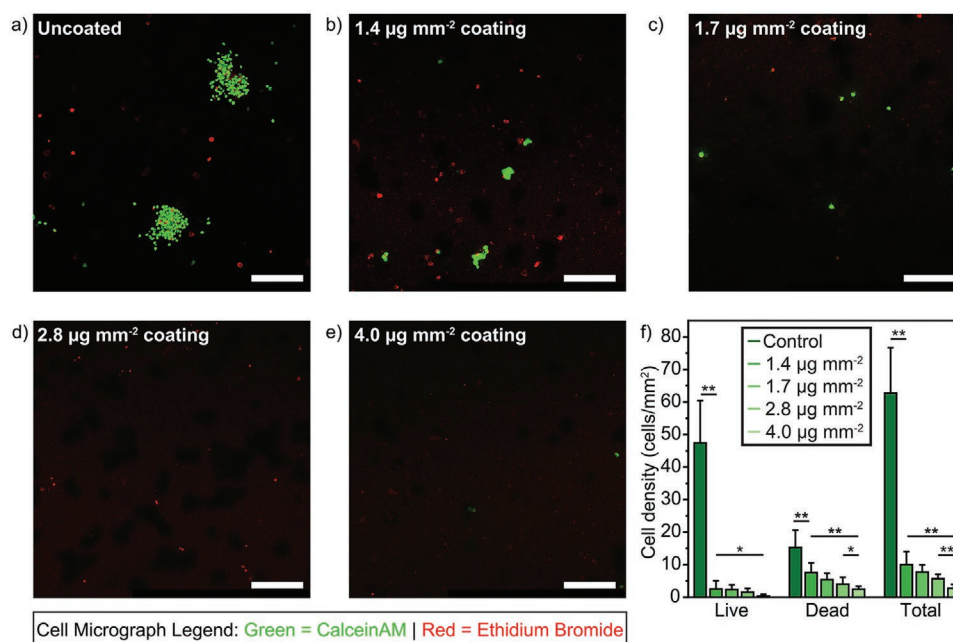


Figure 6. Nanoribbon-coated surfaces show significantly lower adhered cell densities than uncoated controls after 3 d. Fluorescent microscopy images at a 20X magnification of a) an uncoated control and b) 1.4 $\mu\text{g mm}^{-2}$, c) 1.7 $\mu\text{g mm}^{-2}$, d) 2.8 $\mu\text{g mm}^{-2}$, and e) 4.0 $\mu\text{g mm}^{-2}$ nanoribbon coatings illustrate decreasing cell attachment with increasing nanoribbon coating thickness. Scale bars: 250 μm . f) Computational analyses of the fluorescence images reveal statistically significant adhered cell densities between coated and uncoated substrates. Data shown as mean \pm standard error measurement of triplicate wells with 15 different fields for each well. Statistical significance determined by a two-tailed Welch's t-test followed by a Bonferroni correction (*, $p < 0.05$ before Bonferroni correction; **, $p < 0.05$ after Bonferroni correction).

the supernatant. The solution for MALDI-ToF testing was prepared by mixing 25:25:1 (by vol.) of this matrix supernatant, a 1 mg mL^{-1} solution of the zwitterionic amid amphiphile in deionized water, and a 1 mg mL^{-1} solution of SpheriCal Peptide Low (Polymer Factory) in hexane as an internal calibrant. A 3 μL droplet of this MALDI-ToF solution was dried onto a sample plate for analysis. MALDI-MS, m/z : $[\text{M} + \text{H}]^+$ calcd for $\text{C}_{31}\text{H}_{38}\text{N}_4\text{O}_6\text{S}$, 594.251; found, 594.257.

Observing Nanoribbon Self-Assembly: TEM images were captured on an FEI Tecnai G2 Spirit TWIN at an accelerating voltage of 120 kV. To prepare the sample for observation, 5 μL of a 1 mg mL^{-1} solution of assembled ZAAs was pipetted onto a TEM grid (200 mesh, carbon film, Electron Microscopy Sciences), allowed to rest for 20 s, and wicked off with tissue paper. The grid was then stained with 5 μL of 1% phosphotungstic acid solution (Electron Microscopy Sciences) which was pipetted onto the grid, rested for 20 s, and then wicked off.

cryo-TEM images were captured on an FEI Tecnai Arctica microscope at an accelerating voltage of 200 kV and with image defocus between -1.5 and -3.5 μm . Holey carbon grids (Ted Pella, 300 mesh, Cu) were prepared using an FEI Vitrobot Mark IV. A 3 μL droplet of a 2.0 mg mL^{-1} amphiphile solution was pipetted onto the glow-discharged grids in 100% humidity. Grids were blotted for 4 s, plunged into liquid ethane, and stored and imaged in liquid nitrogen.

AFM profiles of nanoribbon assemblies were captured on an Asylum Research Jupiter XR AFM. A silicon substrate was prepared by washing with isopropyl alcohol and drying with N_2 (g). A ZAA nanoribbon solution was diluted to 0.001 wt % and then a 100 μL droplet of this solution was deposited on the cleaned silicon substrate and dried. Nanoribbons were profiled in tapping mode using a AC160 cantilever tip (Asylum, nominal spring constant 25.2 N m^{-1} , 258 kHz resonance frequency).

The SAXS profile of a 1 mg mL^{-1} aqueous solution of nanoribbons in a quartz capillary (2 mm diameter, Hampton Research) was obtained at the Advanced Photon Source at Argonne National Laboratory (beamline 12-ID-B) with a 13.3 keV X-ray radiation energy. A DECTRIS PILATUS 300 K detector captured the 2D X-ray scattering pattern. Beamline software was used to subtract water and capillary background and reduce the pattern to a 1D curve. The data were fit in SasView using

computed X-ray scattering length densities (SLDs) of $9.44 \times 10^{-6} \text{ \AA}^{-2}$ for solvent (water), $9.49 \times 10^{-6} \text{ \AA}^{-2}$ for the amphiphile head group region, and $10.9 \times 10^{-6} \text{ \AA}^{-2}$ for the amphiphile structural domain and tail group region. Fitting was attempted to lamellar, rectangular prism, and cylindrical models which allow for separate SLDs for head and tail group domains. The rectangular prism and cylindrical models fit to nonphysical values based on dimensions observed in TEM and Cryo-TEM, so we selected the lamellar model to extract a nanoribbon thickness.

Surface Coating Properties: SEM images were taken on a Zeiss Merlin High Resolution SEM with a 2 kV accelerating voltage in secondary electron mode. To prepare the sample for observation, a 50 μL droplet of a 1 mg mL^{-1} solution of assembled ZAAs was pipetted onto an SEM stub covered in copper tape and dried. The stub was then coated with a 10 nm Au layer (EMS Q150T ES coater) to prevent sample charging.

Coating thickness was analyzed on a Bruker Dektak DXT-A Stylus profilometer equipped with a 2 μm diameter stylus operating at a 2 mg stylus force. Nanoribbon-coated glass discs were scratched in their centers to reveal the underlying glass surface, and height profiles were captured across these scratches. The film thickness for each coating density is reported as average \pm standard deviation (SD) for $n = 5$ technical replicates.

Contact angle measurements were performed on a Ramé-Hart 500-F1 goniometer. 2 μL droplets of deionized water (high performance liquid chromatography grade) were dispensed onto control and nanoribbon-coated glass coverslips and equilibrated for one minute. Side-view photographs of the droplets were then captured and contact angle was measured on both sides of the water spherical cap using DROPimage Advanced software. Contact angles are reported as average \pm standard deviation for $n = 5$ independent replicates.

Protein Fouling: Aqueous suspensions of ZAA nanoribbons (250, 300, 500, and 700 μg from 1 mg mL^{-1} solutions) were dropcast onto glass discs (15 mm diameter, German glass, Electron Microscopy Sciences) and allowed to dry at room temperature. 100 μL droplets of 1 mg mL^{-1} solutions of BSA and lysozyme in phosphate buffered saline (PBS), and 10x diluted human serum (human male AB plasma, sterile-filtered) were dropcast onto the discs and incubated in a humidified oven at

37 °C for 2 h. Discs were washed four times with PBS and transferred to 24-well plates with 1 mL of 2% w/w sodium dodecyl sulfate (SDS), which were placed on a shake plate for 1 h to detach adsorbed protein. A Micro BCA Protein Assay Kit (ThermoFisher Scientific) was used to determine the concentration of adsorbed protein for each sample. Measurements were taken using a PerkinElmer LAMBDA 850+ UV/Vis spectrophotometer set to 562 nm and averaged between three replicates, with background contributions to the protein assay from nanoribbons desorbed by the SDS detergent solution subtracted from each sample.

Bacteria Culture, Growth, and Imaging: *P. aeruginosa* PAO1 (American type culture collection (ATCC) 15692) from a 20% frozen glycerol stock stored at –80 °C was streaked onto a Luria-Bertani agar (Lennox) petri dish and grown overnight at 37 °C. A single colony was picked, cultured overnight at 37 °C, and shaken at 250 rpm in Cation Adjusted Mueller Hinton-Broth (CAMHB), which is Mueller-Hinton Broth supplemented with 25 µg mL⁻¹ calcium chloride and 12.5 µg mL⁻¹ magnesium chloride.

Biofilm Growth and Staining: Nanoribbons were dropcast into wells of a glass bottom, black chimney 24-well microtiter plate (Grenier Bio) and allowed to dry. Overnight cultures of PAO1 were subcultured in CAMHB for 4–6 h to reach mid-log phase growth and normalized to an optical density (OD₆₀₀) of 0.01. 1 mL of bacterial suspension in 10% CAMHB in 150 × 10⁻³ M sodium chloride was added on top of the dried nanoribbon coating in each of the wells. Biofilms were grown statically in a humid chamber at 37 °C for 48 h.

After 48 h of growth, biofilms were washed three times with 150 × 10⁻³ M sodium chloride, ensuring that 1 mL of sodium chloride is added first before removing 1 mL so as not to dry out the biofilm. On the final wash, 1.1 mL of solution was removed and 100 µL of 20 × 10⁻⁶ M SYTO9 dye was added to each well to stain the microbes. Biofilms were stained statically for 30 min in the dark at room temperature, and then washed again three times with 150 × 10⁻³ M sodium chloride before imaging.

Image acquisition was performed using a confocal laser scanning microscope (LSM 800, Zeiss) with a 63x oil immersion magnification lens, and a step size of 0.5 µm. The excitation wavelength for SYTO9 was set to 488 nm, and fluorophore emission was read at 510 nm. At least three independent wells and five images from each well were taken and analyzed for each condition. Biofilm biomass was quantified using COMSTAT2.^[53,54] Images shown in Figure 5 are Z-stack projections of the maximum intensity, as performed in Fiji.

Cell Attachment and Imaging: All human material work was performed with the approval of the Institutional Review Board of Harvard Medical School. Human astroglia cells SVG-p12 (hASC), obtained from ATCC (US), were described in previous studies.^[58] Cells were grown onto Akron flask (surface 75 cm², vented cap, sterile, Nunclon Delta) in Dulbecco's modified Eagle medium/nutrient mixture F-12 (DMEM/F-12) medium (Gibco) in a low oxygen condition incubator (37 °C, 5% O₂, 5% CO₂, 100% humidity) as a monolayer culture to achieve high density. Upon reaching 80% confluence, cells were passaged using 10X TrypZean and Hank's Balanced Salt Solution (no calcium, no magnesium, ThermoFisher). Cell number and viability were estimated after each passage using Trypan blue and a hemocytometer (Countess II FL Automated Cell Counter, Thermo Fischer scientific). Cells were then replated into a T75 flask at a density of 15 000 cells cm⁻² in DMEM/F12 medium.

10⁵ cells mL⁻¹ suspended in saline or medium (previously described) were pipetted onto nanoribbon-coated or uncoated glass discs. After 3 d of incubation with medium or PBS, cells were incubated with 2.5 × 10⁻⁶ M calcein AM (fluorescein isothiocyanate (FITC) laser line) and 10 × 10⁻⁶ M ethidium bromide (Cy3 laser line) in PBS for 15 min at 37 °C and 5% CO₂. hASC were then washed three times with PBS for 10 min at room temperature. Nanoribbon-coated coverslips were mounted on poly-L-lysine microscope slides (1 mm thickness, 75 mm length, 25 mm width, Thermo Scientific Shandon) with low viscosity slide mounting medium (Fisher Scientific) before imaging with an epifluorescence confocal microscope (Leica SP8, USA), for live/dead imaging.

All samples were analyzed and images were taken using a Leica SP8 confocal microscope. Images were taken with sequential scanning

at 1024 × 1024 resolution with the following laser intensities and characteristics: FITC-HyD at 4.3% with line average of 2 and gain of 107%, Cy3-HyD at 3.9% with line average of 2 and gain of 105%. hASC viability images were taken at 20X magnification with a Z-stack of 50 µm and ten steps and maximum projection was applied as quantification. Cells in 15 randomly selected maximum-projected fields of view were counted with a cell counting and analyzing image processing algorithm.^[59]

Statistical Analysis: Data for the protein fouling experiments are normalized to the UV-vis absorbance intensity of the uncoated substrates as described in the corresponding Methods section. Data are presented throughout the manuscript as the mean ± SD. The number of samples, *n*, is 5 for coating properties and 3 for biofouling experiments, unless specified otherwise. Statistical analyses were completed using a two-tailed Welch's *t*-test followed by a Bonferroni correction, with significance noted as *p* < 0.05 before or after the Bonferroni correction. Statistical analysis was completed in Microsoft Excel and Origin 2020b.

Acknowledgements

The authors thank Dr. Deepti Singh for her assistance in cell preparation and culturing for fluorescence microscopy imaging. The authors also thank Dr. Tiffany Amariuta and Eric Bartell for their assistance with statistical analysis. This material is based upon work supported by the National Science Foundation under Grant No. CHE-1945500. This work was supported in part by the Professor Amar G. Bose Research Grant Program. T.C.-T. acknowledges the support of the Hugh Hampton Young Fellowship and the National Science Foundation Graduate Research Fellowship Program under Grant No. 1122374. E.D.-Y. acknowledges the National Research Foundation, Prime Minister's Office, Singapore for support under its Campus for Research Excellence and Technological Enterprise (CREATE) programme. C.A.C.C. acknowledges the support of the 2021–2022 MathWorks Engineering Fellowship at the Massachusetts Institute of Technology (MIT). This work made use of the Materials Research Science and Engineering Center Shared Experimental Facilities at MIT supported by the National Science Foundation under award number DMR-14-19807 and the MIT Department of Chemistry Instrumentation Facility. X-ray scattering measurements were performed at beamline 12-ID-B of the Advanced Photon Source, a US Department of Energy Office of Science User Facility operated for the US Department of Energy Office of Science by Argonne National Laboratory under Contract No. DE-AC02-06CH11357. This work was performed in part at the Harvard University Center for Nanoscale Systems cryo-TEM facility, a member of the National Nanotechnology Coordinated Infrastructure Network, which was supported by the National Science Foundation under Award No. 1541959. The final panel of the Table of Contents figure was created with BioRender.com.

Conflict of Interest

The authors declare no conflict of interest.

Data Availability Statement

The data that support the findings of this study are available from the corresponding author upon reasonable request.

Keywords

antifouling, self-assembly, supramolecular nanoribbons, surface coatings, zwitterionic

Received: February 9, 2022

Revised: April 22, 2022

Published online: June 30, 2022

- [1] K. Page, M. Wilson, I. P. Parkin, *J. Mater. Chem.* **2009**, *19*, 3819.
- [2] D. Talon, *J. Hosp. Infect.* **1999**, *43*, 13.
- [3] V. B. Damodaran, N. S. Murthy, *Biomater. Res.* **2016**, *20*, 18.
- [4] H. Zhang, M. Chiao, *J. Med. Biol. Eng.* **2015**, *35*, 143.
- [5] G. D. Bixler, B. Bhushan, *Philos. Trans. R. Soc., A* **2012**, *370*, 2381.
- [6] Z. K. Zander, M. L. Becker, *ACS Macro Lett.* **2018**, *7*, 16.
- [7] D. Lindsay, A. von Holy, *J. Hosp. Infect.* **2006**, *64*, 313.
- [8] H. Wake, H. Takahashi, T. Takimoto, H. Takayanagi, K. Ozawa, H. Kadoi, M. Okochi, T. Matsunaga, *Biotechnol. Bioeng.* **2006**, *95*, 468.
- [9] A. Want, M. C. Bell, R. E. Harris, M. Q. Hull, C. R. Long, J. S. Porter, *Biofouling* **2021**, *37*, 433.
- [10] I. Banerjee, R. C. Pangule, R. S. Kane, *Adv. Mater.* **2011**, *23*, 690.
- [11] C. M. Magin, S. P. Cooper, A. B. Brennan, *Mater. Today* **2010**, *13*, 36.
- [12] S. Wieck, O. Olsson, K. Kümmerer, *Environ. Int.* **2016**, *94*, 695.
- [13] J. A. Callow, M. E. Callow, *Nat. Commun.* **2011**, *2*, 244.
- [14] S. B. Levy, B. Marshall, *Nat. Med.* **2004**, *10*, S122.
- [15] "Current HAI Progress Report: 2019 National and State Healthcare-Associated Infections Progress Report", Centers for Disease Control and Prevention, Atlanta, GA **2019**.
- [16] R. M. Klevens, J. R. Edwards, C. L. Richardsjr, T. C. Horan, R. P. Gaynes, D. A. Pollock, D. M. Cardo, *Public Health Rep.* **2007**, *122*, 160.
- [17] M. P. Monopoli, C. Åberg, A. Salvati, K. A. Dawson, *Nat. Nanotechnol.* **2012**, *7*, 779.
- [18] I. Lynch, K. A. Dawson, *Nano Today* **2008**, *3*, 40.
- [19] S. Chen, L. Li, C. Zhao, J. Zheng, *Polymer* **2010**, *51*, 5283.
- [20] J.-M. Zheng, W.-C. Chin, E. Khijniak, E. Khijniak, G. H. Pollack, *Adv. Colloid Interface Sci.* **2006**, *127*, 19.
- [21] P. J. Molino, D. Yang, M. Penna, K. Miyazawa, B. R. Knowles, S. MacLaughlin, T. Fukuma, I. Yarovsky, M. J. Higgins, *ACS Nano* **2018**, *12*, 11610.
- [22] J. L. Dalsin, P. B. Messersmith, *Mater. Today* **2005**, *8*, 38.
- [23] N. A. Alcantar, E. S. Aydil, J. N. Israelachvili, *J. Biomed. Mater.* **2000**, *51*, 343.
- [24] Y. Arima, M. Toda, H. Iwata, *Biomaterials* **2008**, *29*, 551.
- [25] R. Webster, E. Didier, P. Harris, N. Siegel, J. Stadler, L. Tilbury, D. Smith, *Drug Metab. Dispos.* **2007**, *35*, 9.
- [26] P. Zhang, F. Sun, S. Liu, S. Jiang, *J. Controlled Release* **2016**, *244*, 184.
- [27] R. P. Garay, R. El-Gewely, J. K. Armstrong, G. Garratty, P. Richette, *Expert Opin. Drug Delivery* **2012**, *9*, 1319.
- [28] Y. Liu, D. Zhang, B. Ren, X. Gong, L. Xu, Z.-Q. Feng, Y. Chang, Y. He, J. Zheng, *J. Mater. Chem. B* **2020**, *8*, 3814.
- [29] S. Jiang, Z. Cao, *Adv. Mater.* **2010**, *22*, 920.
- [30] J. H. Ortony, B. Qiao, C. J. Newcomb, T. J. Keller, L. C. Palmer, E. Deiss-Yehiely, M. Olvera de la Cruz, S. Han, S. I. Stupp, *J. Am. Chem. Soc.* **2017**, *139*, 8915.
- [31] S. Chen, J. Zheng, L. Li, S. Jiang, *J. Am. Chem. Soc.* **2005**, *127*, 14473.
- [32] J. Baggerman, M. M. J. Smulders, H. Zuilhof, *Langmuir* **2019**, *35*, 1072.
- [33] A. M. Alswieleh, N. Cheng, I. Canton, B. Ustbas, X. Xue, V. Ladmiral, S. Xia, R. E. Ducker, O. El Zubir, M. L. Cartron, *J. Am. Chem. Soc.* **2014**, *136*, 9404.
- [34] B. Li, P. Jain, J. Ma, J. K. Smith, Z. Yuan, H.-C. Hung, Y. He, X. Lin, K. Wu, J. Pfandner, S. Jiang, *Sci. Adv.* **2019**, *5*, eaaw9562.
- [35] A. R. Statz, R. J. Meagher, A. E. Barron, P. B. Messersmith, *J. Am. Chem. Soc.* **2005**, *127*, 7972.
- [36] G. M. Whitesides, J. P. Mathias, C. T. Seto, *Science* **1991**, *254*, 1312.
- [37] S. Zhang, *Nat. Biotechnol.* **2003**, *21*, 1171.
- [38] S. I. Stupp, *Nano Lett.* **2010**, *10*, 4783.
- [39] H. Cui, M. J. Webber, S. I. Stupp, *Pept. Sci.* **2010**, *94*, 1.
- [40] Y. Cho, T. Christoff-Tempesta, S. J. Kaser, J. H. Ortony, *Soft Matter* **2021**, *17*, 5850.
- [41] T. Christoff-Tempesta, Y. Cho, D.-Y. Kim, M. Geri, G. Lamour, A. J. Lew, X. Zuo, W. R. Lindemann, J. H. Ortony, *Nat. Nanotechnol.* **2021**, *16*, 447.
- [42] Y. Cho, T. Christoff-Tempesta, D.-Y. Kim, G. Lamour, J. H. Ortony, *Nat. Commun.* **2021**, *12*, 1.
- [43] J. Drelich, E. Chibowski, *Langmuir* **2010**, *26*, 18621.
- [44] B. B. Haab, B. H. Geierstanger, G. Michailidis, F. Vitzthum, S. Forrester, R. Okon, P. Saviranta, A. Brinker, M. Sorette, L. Perlee, S. Suresh, G. Drwal, J. N. Adkins, G. S. Omenn, *Proteomics* **2005**, *5*, 3278.
- [45] R. T. Ellison3rd, T. J. Giehl, *J. Clin. Invest.* **1991**, *88*, 1080.
- [46] M. Leeman, J. Choi, S. Hansson, M. U. Storm, L. Nilsson, *Anal. Bioanal. Chem.* **2018**, *410*, 4867.
- [47] H.-C. Flemming, J. Wingender, U. Szewzyk, P. Steinberg, S. A. Rice, S. Kjelleberg, *Nat. Rev. Microbiol.* **2016**, *14*, 563.
- [48] H.-C. Flemming, J. Wingender, *Nat. Rev. Microbiol.* **2010**, *8*, 623.
- [49] L. Hall-Stoodley, J. W. Costerton, P. Stoodley, *Nat. Rev. Microbiol.* **2004**, *2*, 95.
- [50] "Antibiotic Resistance Threats in the United States", Centers for Disease Control and Prevention, Atlanta, GA **2019**.
- [51] D. Nathwani, G. Raman, K. Sulham, M. Gavaghan, V. Menon, *Antimicrob. Resist. Infect. Control* **2014**, *3*, 32.
- [52] M. L. Manning, J. Pfeiffer, E. L. Larson, *Am. J. Infect. Control* **2016**, *44*, 1454.
- [53] A. Heydorn, A. T. Nielsen, M. Hentzer, C. Sternberg, M. Givskov, B. K. Ersbøll, S. Molin, *Microbiology* **2000**, *146*, 2395.
- [54] M. Vorregaard, in *Informatics and Mathematical Modelling*, Technical University of Denmark, Kongens Lyngby, Denmark **2008**.
- [55] A. Jana, K. Pahan, *J. Neurosci.* **2010**, *30*, 12676.
- [56] X. Liu, M. Jana, S. Dasgupta, S. Koka, J. He, C. Wood, K. Pahan, *J. Biol. Chem.* **2002**, *277*, 39312.
- [57] W. G. Brodbeck, M. S. Shive, E. Colton, Y. Nakayama, T. Matsuda, J. M. Anderson, *J. Biomed. Mater. Res.* **2001**, *55*, 661.
- [58] S. Henriksen, G. D. Tylden, A. Dumoulin, B. N. Sharma, H. H. Hirsch, C. H. Rinaldo, *J. Virol.* **2014**, *88*, 7556.
- [59] Y. Chen, K. Biddell, A. Sun, P. A. Relue, J. D. Johnson, in *Proc. First Jt. BMES/EMBS Conf. 1999 IEEE Eng. Med. Biol. 21st Annu. Conf. 1999 Annu. Fall Meet. Biomed. Eng. Soc. (Cat. N)*, Vol. 2, IEEE, Piscataway, NJ **1999**, p. 2/819.